3D Printed Designer Color Routers with Low Refractive Index for Low-Light Imaging

Cheng-Feng Pan[1,2], Hao Wang[4,5,*], Bochang Wu[1,2], Max J. H. Tan[1], Shutao Zhang[1,2], Hongtao Wang[1], Wang Zhang[1], Zhenchao Liu[1], Lei Chen[1], Tomohiro Mori[7], Md Abdur Rahman[1], Xiaoyan Zhou[1], Qifeng Ruan[6], Cheng-Wei Qiu[2], Joel K.W. Yang[1,3*]

Affiliations

[1] Engineering Product Development, Singapore University of Technology and Design, Singapore 487372, Singapore

[2] Department of Electrical and Computer Engineering, National University of Singapore, 4 Engineering Drive 3, Singapore, 117576, Singapore

[3] Singapore-HUJ Alliance for Research and Enterprise (SHARE), The Smart Grippers for Soft Robotics (SGSR) Programme, Campus for Research Excellence and Technological Enterprise (CREATE), Singapore 138602, Singapore

[4] School of Instrumentation and Optoelectronic Engineering, Beihang University, Beijing, 100191 China

[5] Hangzhou International Innovation Institute, Beihang University, Hangzhou, 311115, China

[6] Ministry of Industry and Information Technology Key Lab of Micro-Nano Optoelectronic Information System, Harbin Institute of Technology (Shenzhen), Shenzhen 518055, China

[7] Industrial Technology Center of Wakayama Prefecture, Wakayama, 6496261, Japan

Supplementary Note 1: Efficiency of color filter in single sub-pixel and in single unit

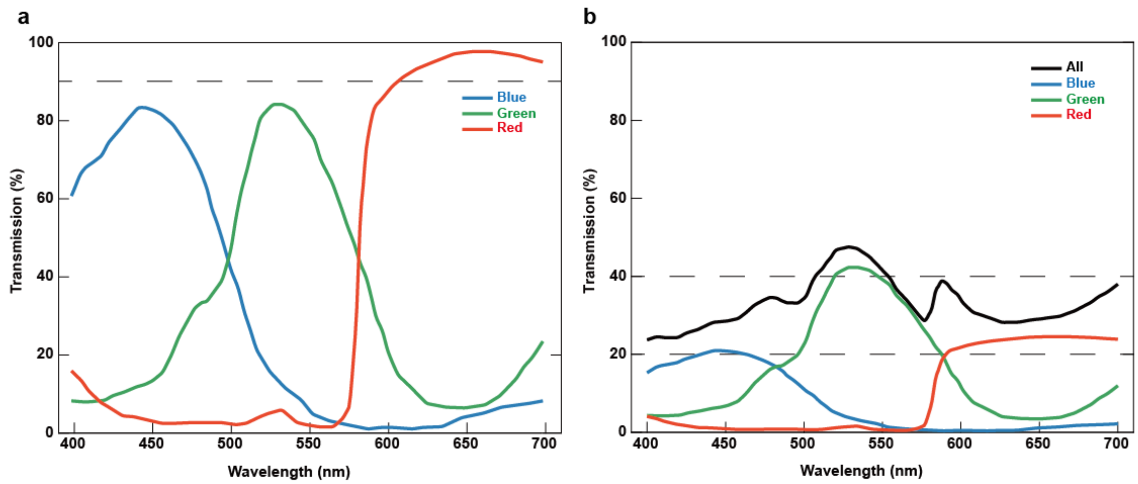

Supplementary Figure 1. Commericialized Fujifilm Color filtering efficiency of the **a.** single pixel in the unit and **b.** the efficiency of the unit (https://www.fujifilm.com/us/en/business/semiconductor-materials/image-sensor-color-mosaic/rgb/applications).

Supplementary Note 2: Fabrication process of the traditional dye based Bayer filter in the industry

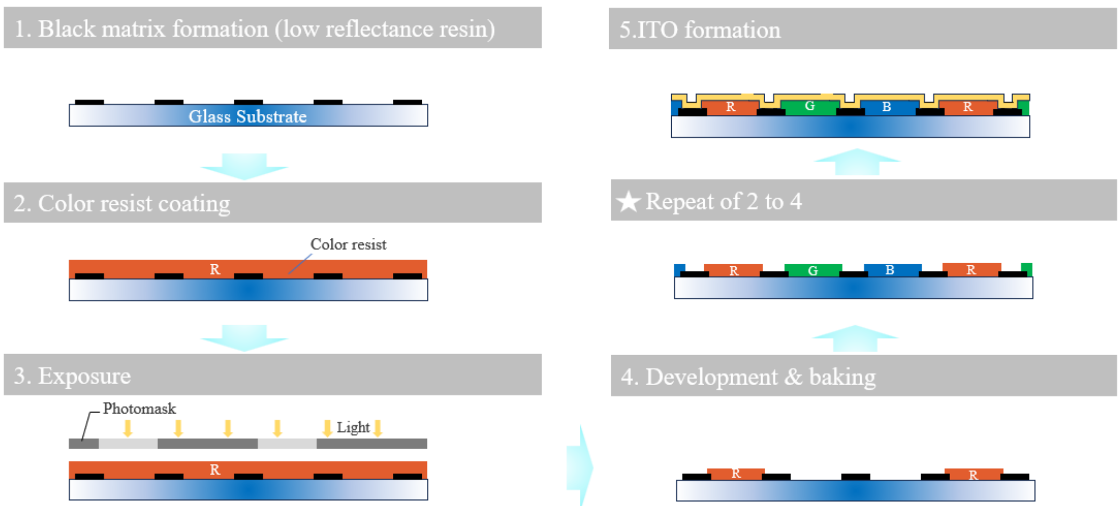

Supplementary Figure 2 Commericialized CMOS filter fabrication process which requires multiple steps to pattern the RGB color filters.

Supplementary Note 3: The second type of 2.5D color router

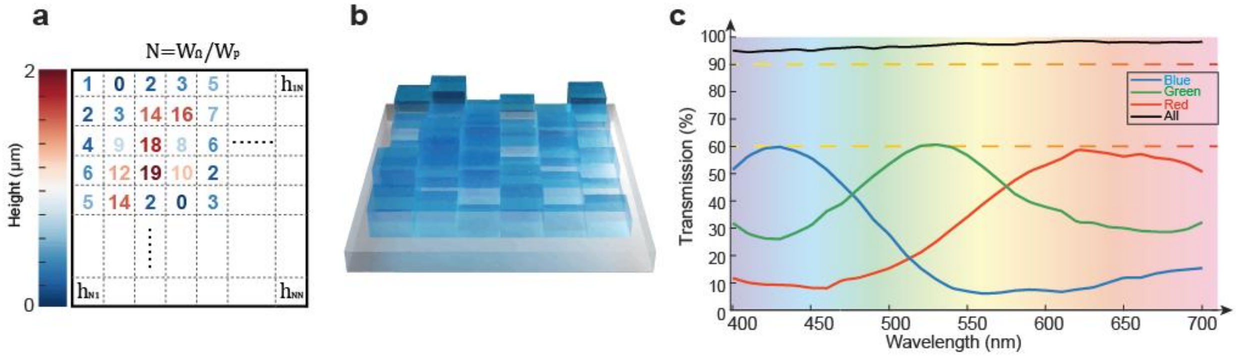

Supplementary Figure 3 Design model and schematic of the optimization region with indicated parameters described in the text. **a-c**. 'Manhattan' Pillars color router (MPCR), **a**. The height parameter matrix H of the pillars, $W_\Omega = 2\ \mu m$ is the design region width, W_p is the width of the pillar, $N = W_\Omega / W_\text{p}$ represents how many pillars in one line and h_nn represents the height of the pillar at line n and row n. b. The schematic of the MPCR. c. We have optimized MPCR for different W_p range from 50 nm to 250 nm and different refractive index (RI), the best results of the color routing spectrum at the focal plane.

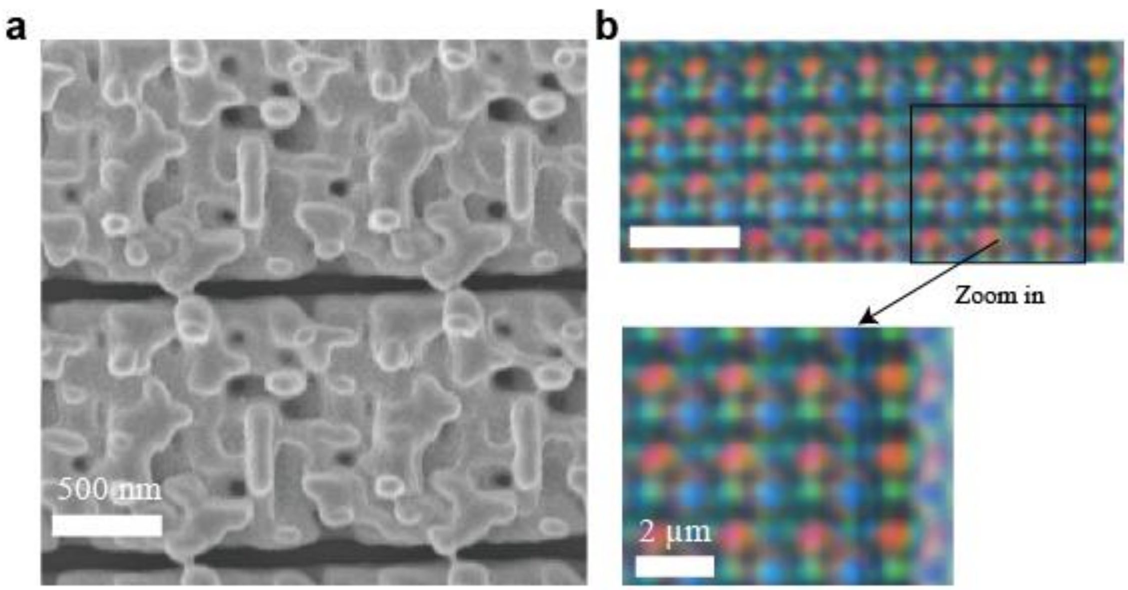

Supplementary Figure 4 Manhatton Pillar Color Router SEM image and routing performance under microscope

Supplementary Note 4: Simulation of structural color of single type nanopillars

A low-index nanopillar array with varying pillar heights and exposure times—which, in two-photon polymerization (TPP) 3D printing, correspond to variations in pillar radius—can exhibit visible structural color under microscope observation, as shown in Supplementary Figure 5 However, the spectrum collected at the designated focal plane does not automatically exhibit separated RGB energy. This result demonstrates that far-field color appearance and near-field routing functionality are governed by different physical mechanisms. The present device should therefore not be regarded simply as a structural-color generator, but rather as a system specifically designed to redistribute optical energy into designated sub-regions at a finite focal distance.

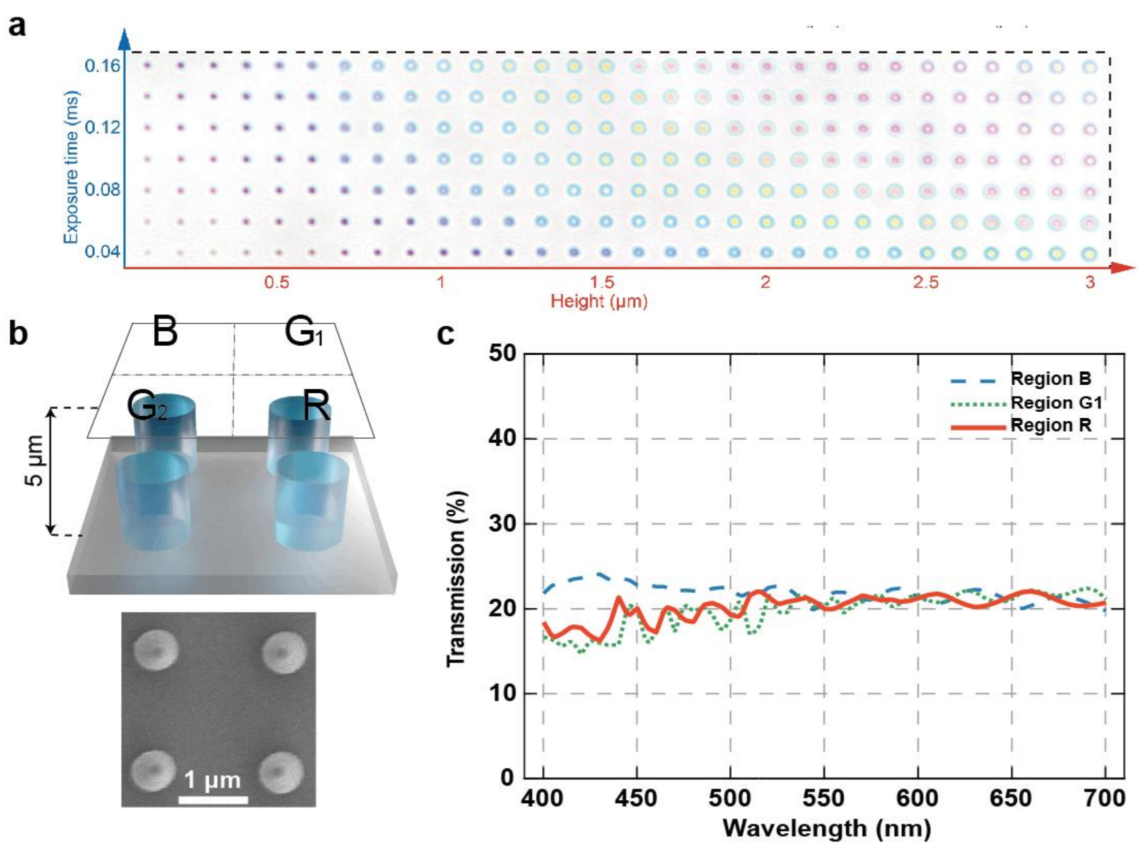

Supplementary Figure 5. a. Optical micrograph of colors from an array of single nanopillars with heights varying from 0.1 to 3 μm (steps of 0.1 μm), and exposure time ranging from 0.04 to 0.16 ms in steps of 0.02 ms, fabricated at laser power of 25 mW. The sample was backlit and imaged using a 50×, NA = 0.4 objective lens. **b.** Schematic of the periodic nanopillar array, in which all nanopillars within each 2 μm period have identical height and radius (top). SEM image of the fabricated nanopillar array with a radius of 200 nm (bottom). **c.** Spectrum collected 5 μm above the incident plane for a periodic nanopillar array in which all pillars have a radius of 250 nm and a height of 1 μm.

Although distinct structural colors are observed in the far field under microscope imaging, no evident color separation is observed in the near field.

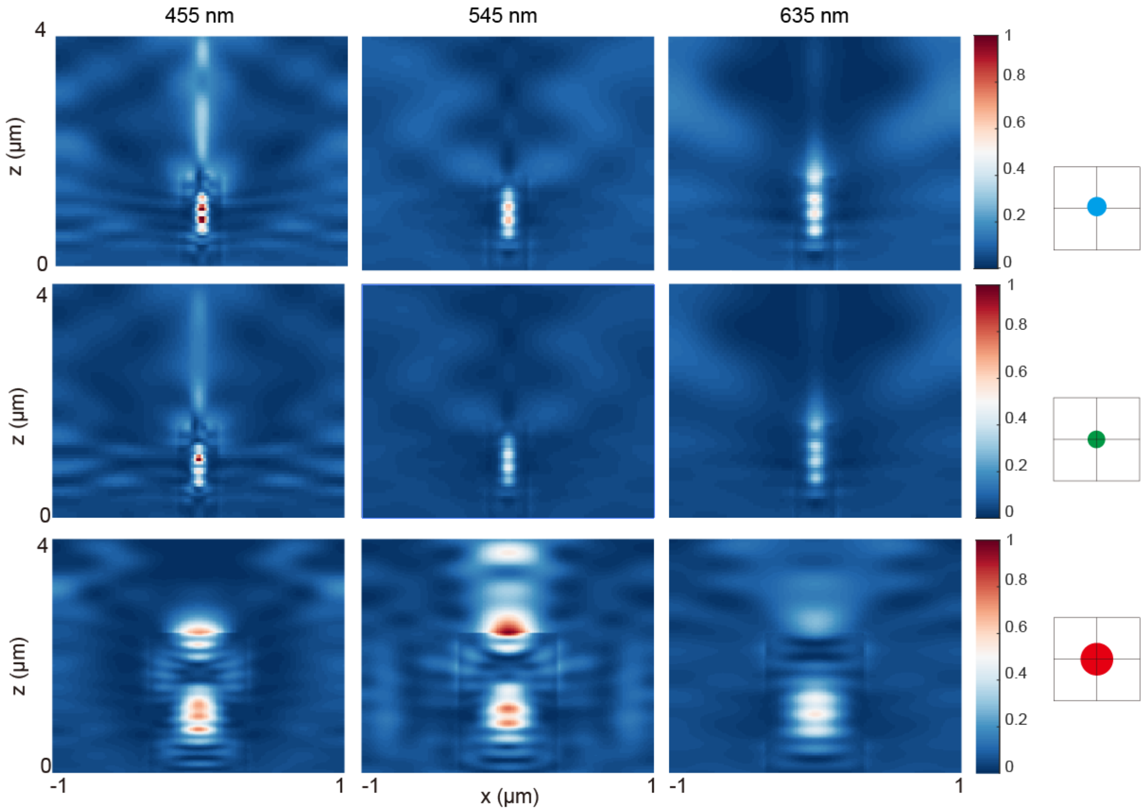

Supplementary Figure 6. Electric-field distributions of periodic nanopillar arrays at different wavelengths. Cross-sectional electric-field intensity profiles are shown for periodic nanopillar arrays under illumination at 455, 545, and 635 nm. Each row corresponds to a different pillar radius, as indicated schematically on the right

Supplementary Note 5: Far field angular distribution of the whole CR and single type of pillars in periodic condition

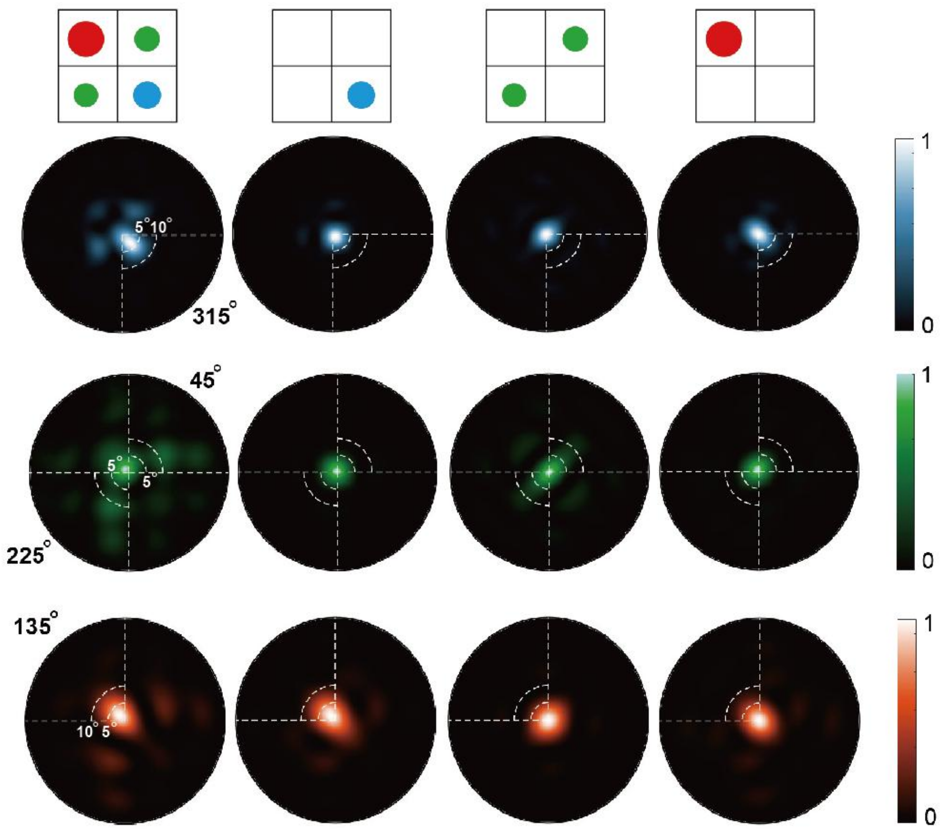

Supplementary Figure 7 The far field pattern of the 3 different types of pillars and the color router unit at 455 nm, 545 nm, and 635 nm.

Supplementary Note 6: Particle Swarm Optimization

In our design, the optimization variables are the radii and heights of three independent pillar types, while the two green pillars are constrained to share the same geometric parameters due to the RGGB symmetry of the device. For each candidate geometry proposed by the particle swarm optimization (PSO) algorithm, full-wave simulations are performed and the routing efficiencies at the three target wavelengths are extracted. The objective function is defined as the minimum of the three channel efficiencies,

$$T_\lambda = \frac{\int_{A_\lambda} I_\lambda dx dy}{\int_{A_0} I_\lambda dx dy} \qquad \lambda = R\ (635\ nm), G(G1 + G2)\ (545\ nm), B\ (455\ nm)$$

$$T = Max(Min(T_\lambda))$$

T_λ denote the efficiencies at the selected red, green, and blue wavelengths, respectively. This max–min formulation was chosen to avoid solutions that favor only one or two channels and instead enforce balanced RGB routing performance.

A standard PSO scheme was used. For the ith particle at iteration the velocity and position were updated according to

$$\boldsymbol{v}_i^{t+1} = \omega \boldsymbol{v}_i^t + c_1 r_1 (\boldsymbol{p}_i^t - \boldsymbol{x}_i^t) + c_2 r_2 (\boldsymbol{p}_i^t - \boldsymbol{x}_i^t)$$

$$\boldsymbol{x}_i^{t+1} = \boldsymbol{x}_i^t + \boldsymbol{v}_i^{t+1}$$

Where $\boldsymbol{x}_i$ and $\boldsymbol{v}_i$are the geometric-parameter vector and velocity of particle i, ω is the inertia weight, c_1 and c_2 are the cognitive and social coefficients, r_1 and r_2 are random numbers uniformly distributed in [0,1], $\boldsymbol{p}_i$ is the personal-best solution of particle i , and $\boldsymbol{g}$ is the global-best solution. The optimization starts from randomly initialized particles within prescribed geometric bounds. All particle parameters were imported from MATLAB into Ansys Lumerical, where scripts were used to automatically generate the corresponding structures and run the electromagnetic simulations. After each simulation, the transmitted intensity within the selected detection regions at the three target wavelengths was extracted in Lumerical and transferred back to MATLAB. Based on the calculated objective value, we then determined whether the updated result represented the personal best for each particle or the global best across the swarm. Once all particles had been evaluated, the design parameters were updated according to the standard PSO equations for the next iteration. The inverse design was carried out iteratively until convergence was reached. During the optimization, the pillar radius was constrained to the range of 0.08–0.5 µm. The lower bound was set by the fabrication resolution of our system, while the upper bound was determined by the size of the predefined sub-region (1 µm). The radius increment was set to 10 nm. The pillar height was constrained to the range of 0–3 µm. The upper height limit was chosen by considering the mechanical stability of the structures, since excessively tall pillars with large aspect ratios are more likely to collapse during fabrication or subsequent processing.

In our equations, the stochastic terms r_1 and r_2 are retained in the standard PSO update, so random variation is naturally included in the search process. The iteration proceeds until convergence, defined by the stage at which the global best objective value shows negligible improvement over successive iterations.

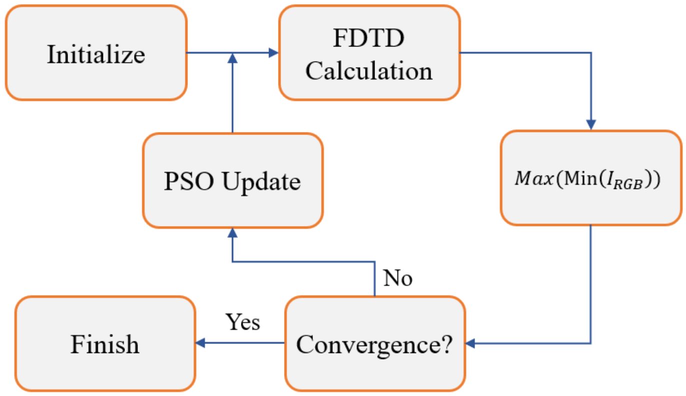

Supplementary Figure 8 The inverse design flow of the Particle Swarm Optimization method.

To reduce the possibility of trapping in a poor local optimum, we used swarm-based global exploration rather than a local gradient-based optimizer. In addition, the final optimized design was further checked by post-optimization parameter sweeps, including variations in pillar spacing and height, which showed that moving away from the reported geometry leads to degraded performance as discussed in comments 9. This supports that the reported solution is robust and corresponds to a physically meaningful optimum under the chosen design constraints.

Supplementary Note 7: CR performance with different incident angle

Focal-plane intensity measurements of the color router under a series of oblique incidence angles (0°, 2°, 4°, 6°, 10°, 14°, 18°, and 22°). These measurements directly visualize the evolution of the routed RGB focal patterns under tilted illumination. To quantify the image degradation observed in these data, we further extracted an assignment-accuracy metric from the focal-plane images, defined as the fraction of target sub-pixel regions that remain correctly assigned to their intended color channels. This provides an image-level measure of angle-induced distortion and channel mixing.

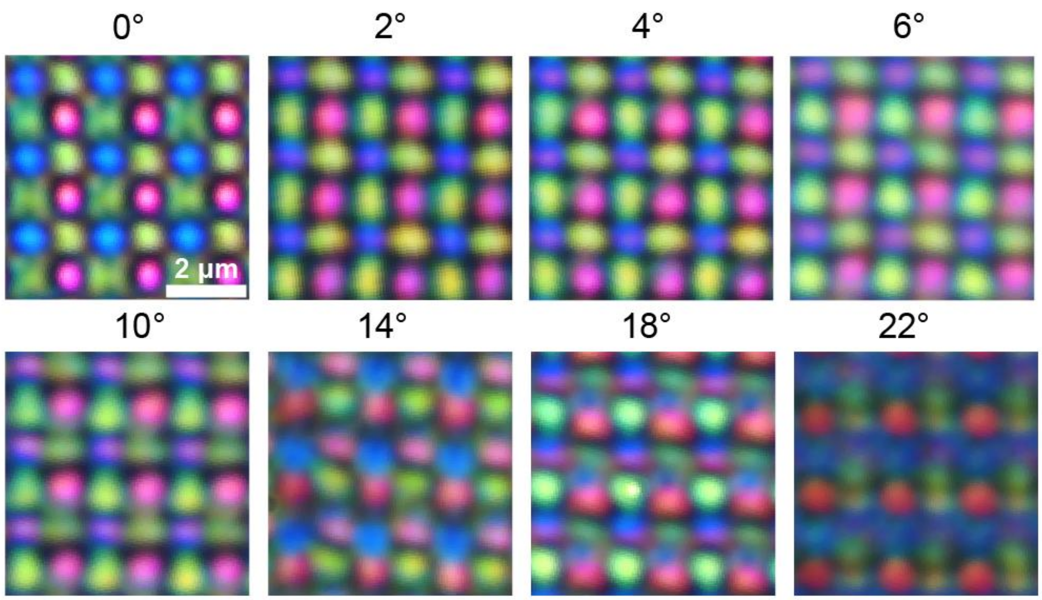

Supplementary Figure 9. Experiment focal-plane intensity distributions of the CR for different incident angles of 0°, 2°, 4°, 6°, 10°, 14°, 18°, and 22°. The images show the evolution of the routed RGB spot patterns as the illumination angle increases. With increasing oblique incidence, the focal spots become broader and less localized, and the spatial separation between neighboring color channels is gradually reduced.

Second, to consider the full angular response curves across all RGB channels, we performed wavelength-resolved simulations of the three-channel transmission as a function of incident angle. For each angle, the transmitted power collected in the designated focal-plane region of each channel was extracted and normalized, yielding the angular response of the blue, green, and red channels rather than that of only a single representative wavelength or a single routing channel. Based on this data, we further calculated channel purity and crosstalk as quantitative illustration of angular robustness. Here, channel purity describes the fraction of collected signal that remains in the intended channel, whereas crosstalk quantifies the relative leakage from non-target channels.

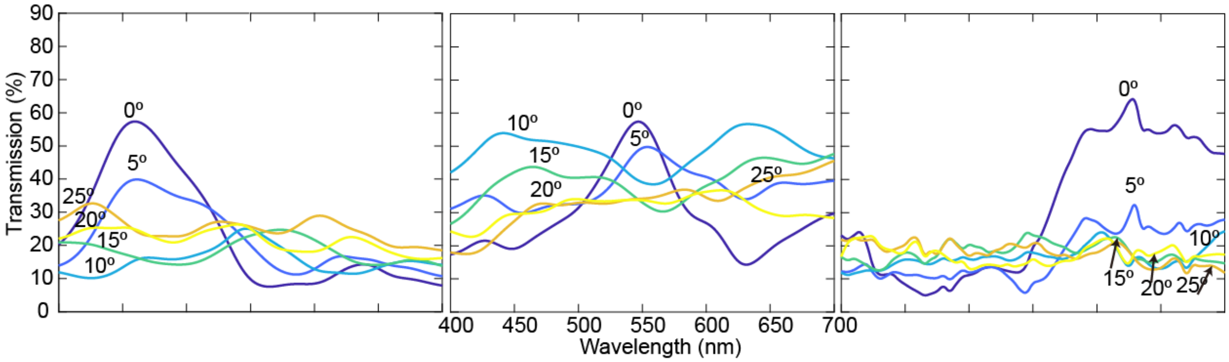

Supplementary Figure 10. Simulated transmission spectra of the blue, green, and red routing channels under different incident angles. For each channel, the transmitted power collected in the corresponding target focal-plane region is plotted as a function of wavelength for incident angles from 0° to 25°. The results show that increasing incident angle modifies both the spectral response and the peak transmission of each channel, indicating angle-dependent degradation in channel selectivity and routing efficiency.

Supplementary Note 8: Shrinkage compensation and weak fabrication sensitivity

During fabrication, a MATLAB script was developed to convert the design parameters—including pillar height, scan speed, exposure dose, and period—into GWL instruction files for the Nanoscribe system, thereby controlling both the scanning path of the femtosecond pulsed laser and the motion of the piezoelectric stage. Prior to printing the CR arrays, routine scan-speed and dose calibration tests were performed to determine the optimal fabrication conditions[1].

The nanopillars were fabricated in a layer-by-layer manner. For example, a pillar with a height of 1.2 µm was printed in four layers, each 400 nm thick, with an overlap of 100 nm between adjacent layers. This overlap does not noticeably affect the final geometry, but it improves the mechanical robustness of the structure. Laterally, each circular pillar was written from the center outward using concentric circular scans with a radial step of 50 nm. For instance, a pillar with a nominal radius of 200 nm was written using four concentric rings. To account for radical diffusion and proximity effects, the written radius was manually reduced by approximately 20–40 nm, depending on the feature size and printing conditions. In addition, a waiting time of about 0.01 ms was introduced between successive layers and rings to allow sufficient radical diffusion before the next exposure step.

Shrinkage compensation was implemented as a practical geometric pre-adjustment based on the dimensional deviations observed after fabrication, rather than through a fully predictive dose-to-shrinkage model. In other words, the designed dimensions were empirically corrected according to the measured tendency of the printed structures to contract during processing, and the final geometry was then verified by SEM inspection. We acknowledge that this procedure was not described clearly enough in the original manuscript.

More specifically, after the first fabrication round, the fabricated pillar heights and radii were characterized by SEM and compared with the design values. Based on the measured deviations, manual geometric compensation was introduced into the writing code: dimensions that were consistently larger than designed were reduced in the input pattern, whereas those that were smaller were correspondingly increased. This iterative correction was used to compensate for systematic fabrication offsets. To further improve structural fidelity and reduce proximity-related distortion during printing, additional waiting time was introduced between successive printed layers to allow sufficient radical diffusion, thereby mitigating proximity effects and promoting more complete polymerization. After development, while immersed in isopropyl alcohol, the sample was further cured under UV illumination for 5 min at 70% maximum power (DYMAX MX-150, 405 nm), which improved the mechanical rigidity and stability of the final structures.

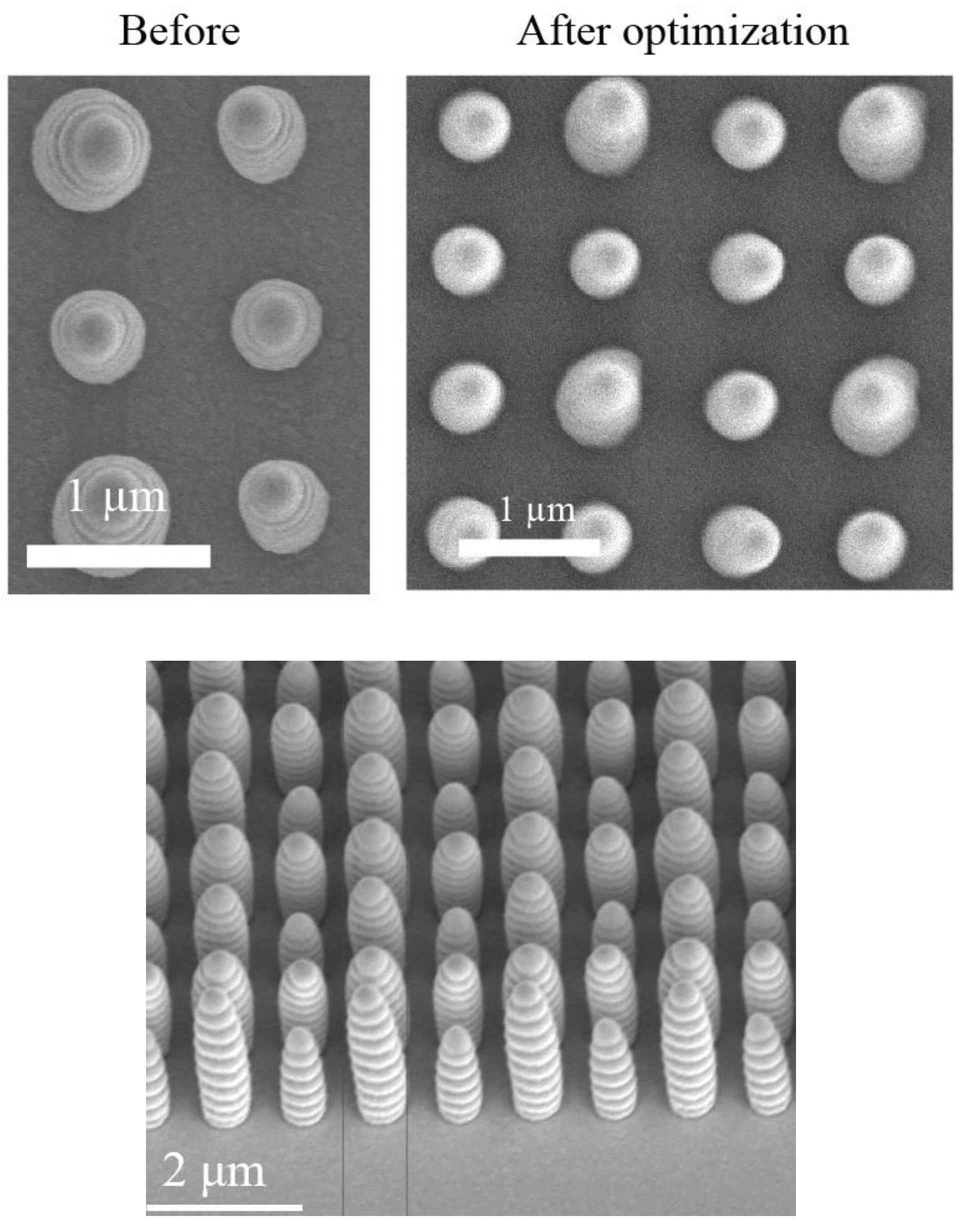

Supplementary Figure 10. The SEM images of the CR before and after optimization in the top view and with tilting angle.

In addition, recent advances in two-photon polymerization lithography have significantly improved dimensional control and fabrication precision[2, 3]. In our work, the structures were fabricated using a Nanoscribe GT system. According to the manufacturer's specifications, the stage-control precision can reach approximately 10 nm in the vertical direction, while the lateral resolution is on the order of 200 nm. Combined with the relatively low sensitivity of the present low-index design to moderate dimensional variation, this level of fabrication precision supports the practical robustness of the proposed device.

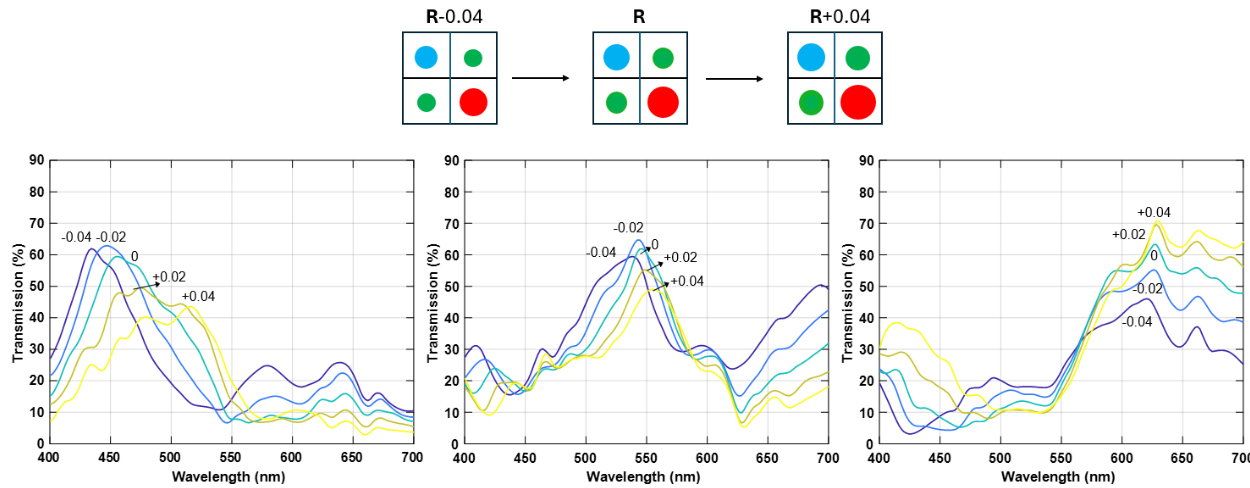

Supplementary Figure 11. Influence of the radius variation of the red nanopillar on the spectral transmission of the RGB channels at the focal plane. The top row schematically illustrates the gradual change in the pillar radiuses **R** = [0.28, 0.24, 0.34, 0.24] µm from **R** − 0.04 µm to **R** and **R** + 0.04 µm. The bottom panels show the corresponding transmission spectra collected in the blue, green, and red detection regions, respectively, for different radius offsets.

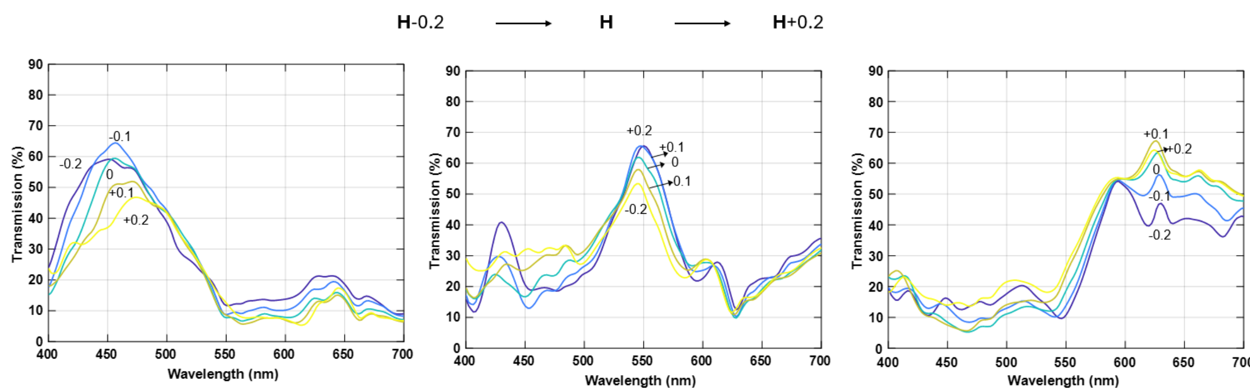

Supplementary Figure 12. Influence of the height variation of the selected nanopillar on the spectral transmission of the RGB channels at the focal plane. The top words mean that the gradual change in pillar height **H** = [1.2,1.9,2,1.9] µm from **H** − 0.2 µm to **H** and **H** + 0.2 µm. The bottom panels show the corresponding transmission spectra collected in the blue, green, and red detection regions, respectively, for different radius offsets.

Supplementary Note 9: Optimization of the same height color router

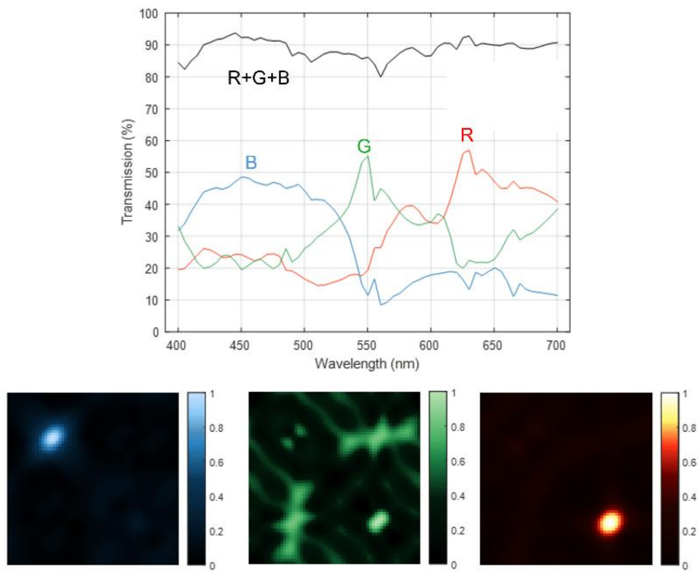

Supplementary Figure 14. In simulation we inverse designed the low RI CR with the same height of 2 µm. The top row is the spectrum of the same height CR and the bottom is the simulated results of the electric field at the focal plane.

Supplementary Note 10: Video

Included in supplementary video 1.

Z-axis-dependent color-routing performance under white-light illumination. The video shows the optical response of the 3D-printed low-index color router recorded by optical microscopy while the focal plane is scanned along the z axis. As the imaging plane moves away from the structure, the initially unseparated white-light pattern gradually evolves into a clearly resolved RGGB color-routing pattern, demonstrating successful spatial separation of red, green, and blue light.

Supplementary Note 11: Color comparison on the CIE coordinate

Table 1. Color difference and RGB value demonstrated in Figure. 4a and b

Name	R	G	B	Normalized error
White				
Ground truth	1	1	1	
Color router	1	1	1	0
Color filter	0.95	0. 92	1	0.094
Yellow-Green				
Ground truth	0.5	1	0	
Color router	0.35	1	0.2	0.245
Color filter	0.42	1	0.3	0.31
Red				
Ground truth	1	0	0	
Color router	1	0.08	0.03	0.08
Color filter	1	0.2	0.14	0.24
Blue				
Ground truth	0	0	1	
Color router	0.02	0.1	1	0.1
Color filter	0.1	0.12	1	0.156
Yellow				
Ground truth	1	1	0	
Color router	0.87	1	0.05	0.13
Color filter	0.87	1	0.22	0.25

The color reconstruction process is discussed below. For each RGGB unit cell, the monochrome sensor records grayscale intensities corresponding to the routed spectral components in the R, G_1, G_2, B sub-pixel regions. The recorded intensity in channel k can be expressed as

$$I_k = \int_{\lambda} S(\lambda)O(\lambda)R_k(\lambda)Q(\lambda)d\lambda$$

Where $S(\lambda)$ is the illumination spectrum, $O(\lambda)$ is the object spectral response, $R_i(\lambda)$ is the spectral routing response of the CR for channel k, $Q(\lambda)$ is the detector quantum efficiency. Th four grayscale values within one RGGB unit cell are then assembled into a measurement vector,

$$\boldsymbol{i} = [I_R, I_G, I_B]^T,$$

We use the projected white color as the normalized white, Normalize:

$$\boldsymbol{c}_{norm} = \frac{\boldsymbol{i}}{\boldsymbol{i}_{white}} = \begin{bmatrix} R \\ G \\ B \end{bmatrix}$$

Transfer from linear RGB to XYZ(D65)

$$\begin{bmatrix} X \\ Y \\ Z \end{bmatrix} = 100 \begin{bmatrix} 0.4124564 & 0.3575761 & 0.1804375 \\ 0.2126729 & 0.7151522 & 0.0721750 \\ 0.0193339 & 0.1191920 & 0.9503041 \end{bmatrix} \begin{bmatrix} R \\ G \\ B \end{bmatrix}$$

XYZ to CIELAB:

$$L^* = 116\left(\frac{Y}{Y_n}\right) - 16$$

$$a^* = 500[\left(\frac{X}{X_n}\right) - \left(\frac{Y}{Y_n}\right)]$$

$$b^* = 200[\left(\frac{Y}{Y_n}\right) - \left(\frac{Z}{Z_n}\right)$$

The color difference was then calculated as:

$$\Delta E_{ab}^* = \sqrt{(L_{\mathrm{CR}}^* - L_{\mathrm{GT}}^*)^2 + (a_{\mathrm{CR}}^* - a_{\mathrm{GT}}^*)^2 + (b_{\mathrm{CR}}^* - b_{\mathrm{GT}}^*)^2}.$$

Where CR refers to color router and GT refers to the ground truth.

Table 2. Reconstructed color interpreted in sRGB and in CIELAB of colors in Figure. 4a and b

Color sample	**GT RGB**	**CR RGB**	**GT *(L*, a*, b*)***	**CR *(L*, a*, b*)***	**ΔE***
White	(1, 1, 1)	(1, 1, 1)	(100, 0, 0)	(100, 0, 0)	0
Yellow green	(0.5, 1, 0)	(0.35, 1, 0.2)	(89.89, −67.93, 85.80)	(88.70, −75.78, 76.93)	11.89
Red	(1, 0, 0)	(1, 0.08, 0.03)	(53.24, 80.09, 67.20)	(53.81, 78.54, 65.57)	2.32
Blue	(0, 0, 1)	(0.02, 0.10, 1)	(32.30, 79.19, −107.86)	(33.91, 74.44, −105.15)	5.70
Yellow	(1, 1, 0)	(0.87, 1, 0.05)	(97.14, −21.55, 94.48)	(94.76, −34.86, 90.74)	14.02

Supplementary Note 12: Color comparison on the CIE coordinate

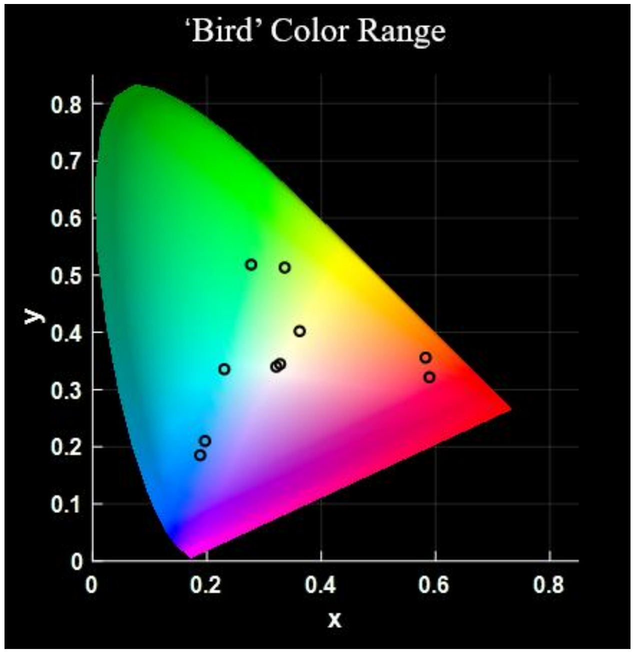

Supplementary Figure 13. The range of colors we have used in the 'Bird' image which is plotted on the CIE coordinate.

Supplementary Note 13: Quantum efficiency of the monochrome and colorful camera

The monochrome and color cameras used in our comparison are FLIR BFS-U3-200S6M and BFS-U3-200S6C, respectively. According to the manufacturer's datasheets as shown in Table 1, both cameras use the same underlying Sony IMX183 CMOS sensor, with identical resolution and pixel size, and very similar EMVA 1288 performance metrics, including maximum signal-to-noise ratio and absolute sensitivity threshold. The essential difference is that the color version integrates a Bayer color filter array on top of the same sensor, whereas the monochrome version does not. In this sense, the monochrome camera represents the intrinsic sensor response, while the color camera represents the response of the same sensor combined with a conventional color filter array.

https://softwareservices.flir.com/BFS-U3-200S6/latest/EMVA/EMVA.html

Table 2: EMVA 1288 Imaging Performance

	BFS-U3-200S6M	**BFS-U3-200S6C**
Resolution	5472 x 3648	5472 x 3648
Sensor	Sony IMX183, CMOS 1"	Sony IMX183, CMOS 1"

Pixel Size (µm)	2.40	2.40
Signal to Noise Ratio Maximum (dB)	41.71	41.84
Absolute Sensitivity Threshold (e-)	3.80	3.79

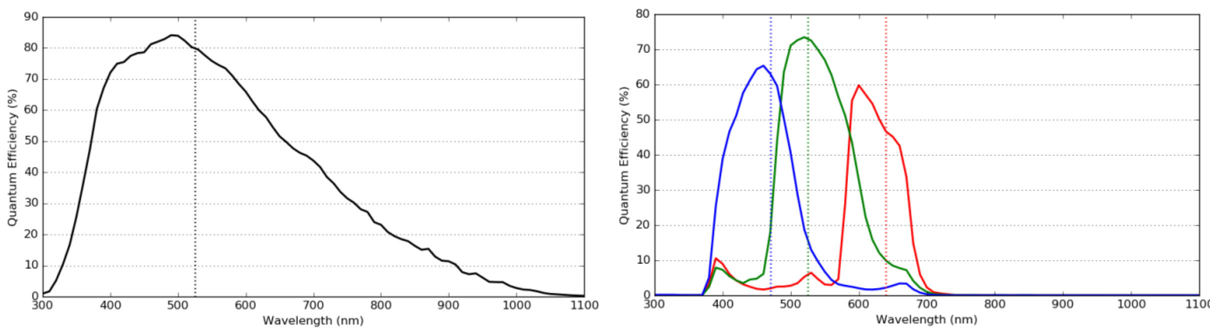

Supplementary Figure 16. Quantum efficiency of the monochrome and colorful camera

Supplementary Note 14: Optical Setup

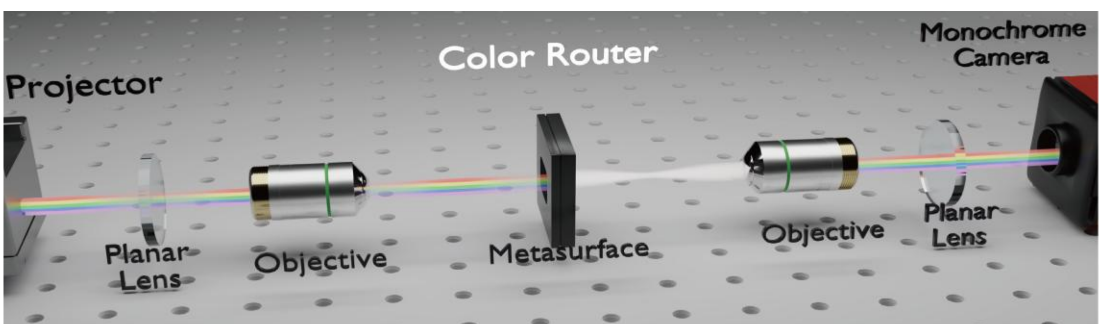

Supplementary Figure 17. Optical Setup of the imaging process of the CPCR.

Supplementary Note 15: Ground truth of the figure in Figure. 4d

The reconstruction error is calculated for the color in the CR/CF. After we use the code to selected out the different colors and the their RGB value inside the original image. Later once we get the reconstructed images, we selected out the color at the same position and obtained the rgb. After we calculated the distances between RGB and rgb. The largest distance error is $\sqrt[2]{3}$ which is the distance between (1,1,1) to (0,0,0). So the distance is directly used as the error rate.

$$e = \frac{\sum_{i=1}^{n}\sqrt{(R_i - r_i)^2 + (G_i - g_i)^2 + (B_i - b_i)^2}}{n * \sqrt[2]{3}}$$

CF: average error rate: 20%

CPCR: average error rate: 8%

Supplementary Note 16: Polarization dependence

We have added polarization-resolved analysis of both the routing efficiency and the color-separation behavior. Because the optimized CR geometry is anisotropic and not fully rotationally symmetric, its optical response is expected to vary under orthogonal incident polarizations. We therefore separately evaluated the device under x- and y-polarized illumination. As shown by the polarization-resolved transmission spectra, the overall RGB routing functionality is preserved for both polarizations. The corresponding focal-plane intensity distributions further confirm that the intended wavelength-dependent spatial routing is maintained under both polarization states, although the spot shape, localization, and field distribution vary between x and y polarization.

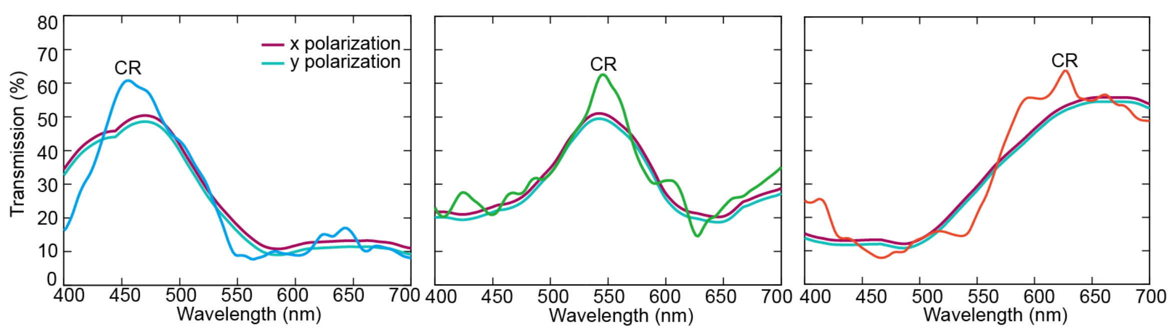

Supplementary Figure 14. Polarization-resolved transmission spectra of the color router (CR) for the blue, green, and red routing channels under x- and y-polarized and x+y polarized incidence. The three panels show the transmitted power collected in the corresponding target focal-plane regions for the blue, green, and red channels, respectively.

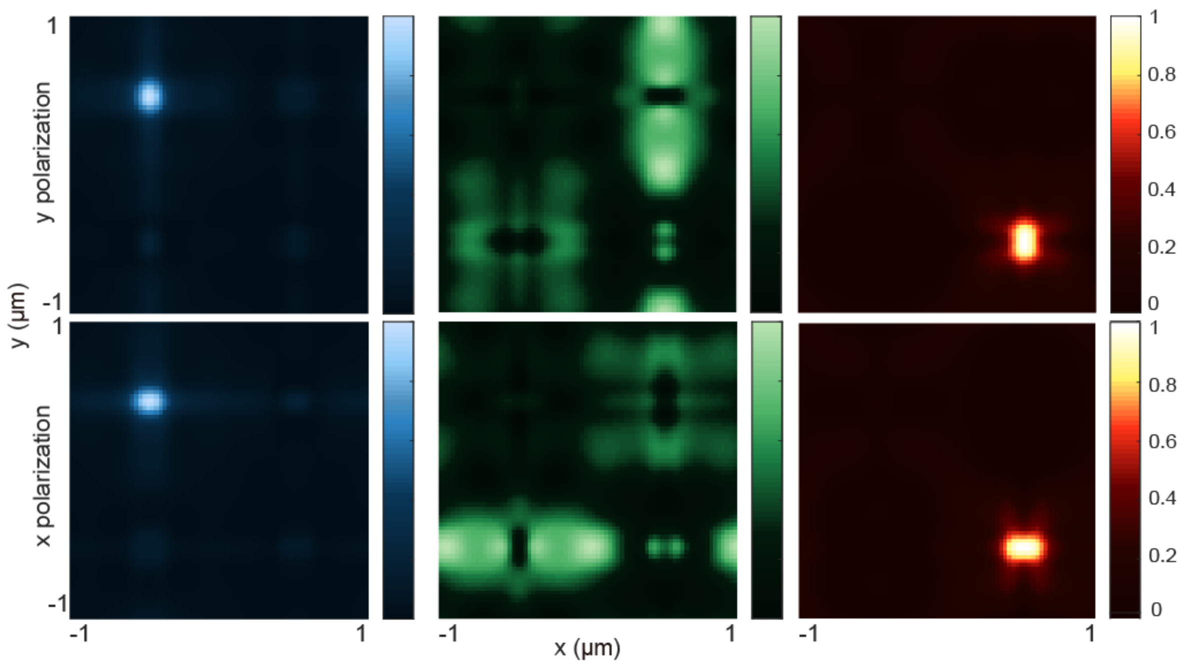

Supplementary Figure 15. Polarization-resolved focal-plane intensity distributions of the color router (CR) for y-polarized (top row) and x-polarized (bottom row) illumination at the blue, green, and red target wavelengths. The columns correspond to the routed intensity patterns for the blue, green, and red channels, respectively.

Supplementary Note 17: Influence of the bandwidth of different channels:

We have added an analysis of the camera raw color space under different RGB bandwidth conditions[4]. Broader passbands primarily lead to inter-channel crosstalk, rather than an inevitable collapse of the final color gamut. In practice, this crosstalk can be mitigated by matrix-based color correction using a calibrated response matrix, while standard post-processing steps such as white balancing and color correction can further reduce chromatic deviations in reconstructed images. Accordingly, the effect of broader routing spectra should be assessed at the system level, rather than inferred solely from the optical bandwidth.

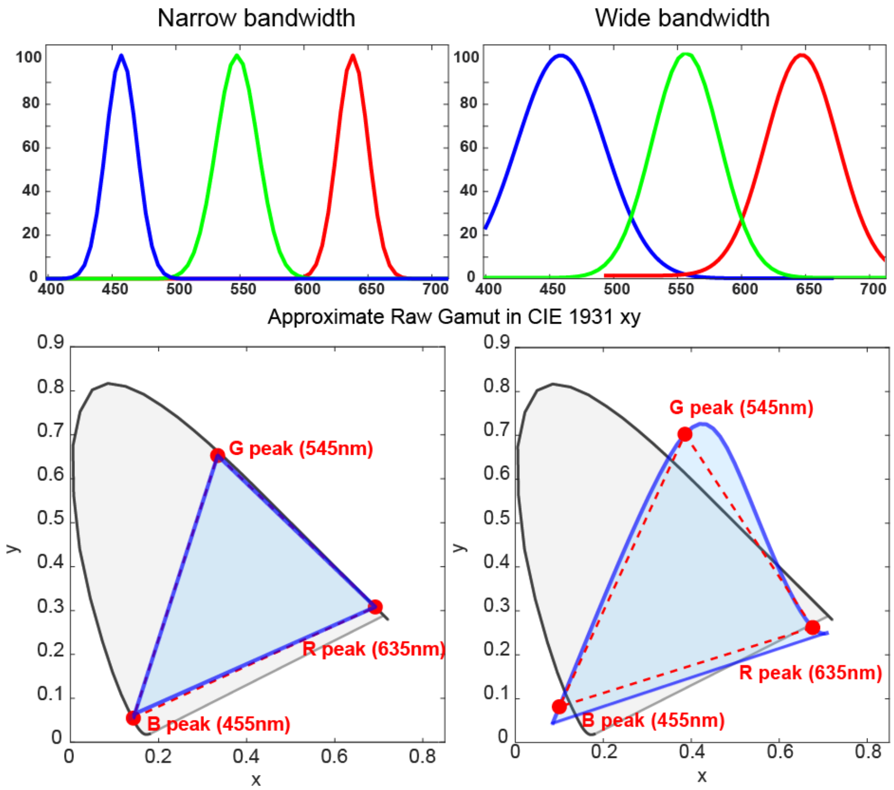

Supplementary Figure 20. Effect of RGB filter bandwidth on the achievable camera raw color gamut. Top panels show two representative sets of normalized RGB spectral response curves with different full width at half maximum (FWHM): narrow-band filters (left) [30, 40 ,30] nm and wide-band filters (right) [100, 70, 140] nm for RGB. Bottom panels show the corresponding approximate camera raw gamut in the CIE 1931 xy chromaticity diagram, constructed from the peak-response wavelengths of the blue, green, and red channels (455 nm, 545 nm, and 635 nm, respectively). The shaded triangle indicates the raw color gamut defined by the three channel responses. Compared with wide-band filters, narrow-band filters produce more spectrally selective channel separation and thus a larger and more well-defined raw color gamut, whereas broader filters introduce stronger spectral overlap and lead to a reduced and distorted gamut but overall, there are small distortions caused by the wider FWHM.

Supplementary Note 18: Influence of 30 nm ITO layer:

In our device, the ITO layer is located between the low-index resin structure and the substrate. It was introduced primarily as an interface-assisting layer for fabrication. In the Nanoscribe system, the substrate interface is identified through the reflected signal associated with the refractive-index contrast between the photoresist and the underlying material. To provide a clearer and more reliable interface signal during focusing and alignment, a thin ITO layer was deposited on the substrate. In the present work, the ITO thickness is only 30 nm, so its influence on the overall optical response is limited. Nevertheless, because ITO has a refractive index different from that of the surrounding dielectric layers, its presence slightly modifies the interfacial reflection and transmission conditions, which in turn introduces a measurable effect on the optical performance.

This is why our simulations show that removing the ITO layer leads to improved overall transmission and routing efficiency.

To clarify its influence, we have now provided a direct comparison between the original structure and the case with ITO removed. We also include the comparison of the overall transmission for 30 nm ITO + silica substrate versus pure silica substrate. From these results, it can be clearly seen that removing the ITO leads to an obvious improvement in both the device performance and the overall transmission.

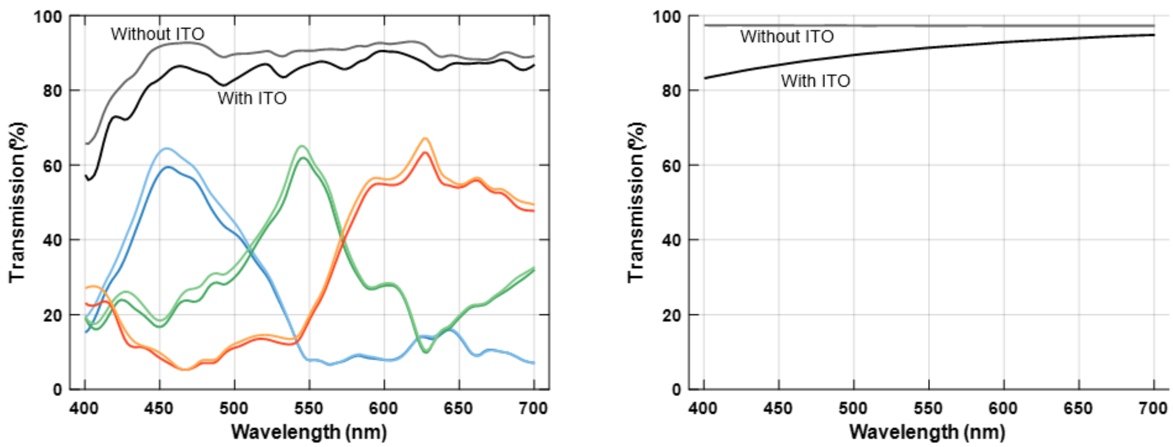

Supplementary Figure 21. Comparison of the simulated transmission spectra of the color router with and without the 30 nm ITO layer (left). The colored curves correspond to the routed transmission into the R, G, and B output regions, and the black curves show the overall transmission. Comparison of the simulated broadband transmission through the substrate stack with 30 nm ITO on silica and pure silica only (right), indicating the parasitic transmission loss introduced by the ITO layer.

The physical reason is that the ITO layer introduces additional parasitic optical loss and modifies the optical response of the substrate stack. Compared with a pure silica substrate, the presence of the 30 nm ITO layer causes extra attenuation of the transmitted light and slightly perturbs the field propagation through the structure. As a result, less optical power reaches the desired output regions, which lowers the measured routing efficiency and total transmission. When the ITO is removed, these unwanted losses are reduced, leading to higher throughput and improved routing performance.

Supplementary Note 19: Influence in low light conditions:

In order to demonstrate the performance of CR in low light scenarios, we performed two sets of low-light measurements. First, we examined the reconstructed color images under progressively reduced illumination power, from 312.5 μW/cm^2 down to 12.5 μW/cm^2, as shown in Supplementary Figure 18. The results show that recognizable color patterns can still be separated and observed as the illumination is decreased, although the image brightness and color distinctiveness gradually degrade at very low input power due to the reduced signal-to-noise ratio. This directly demonstrates the operational behavior of the CR device under low-illumination conditions rather than under only bright-field conditions.

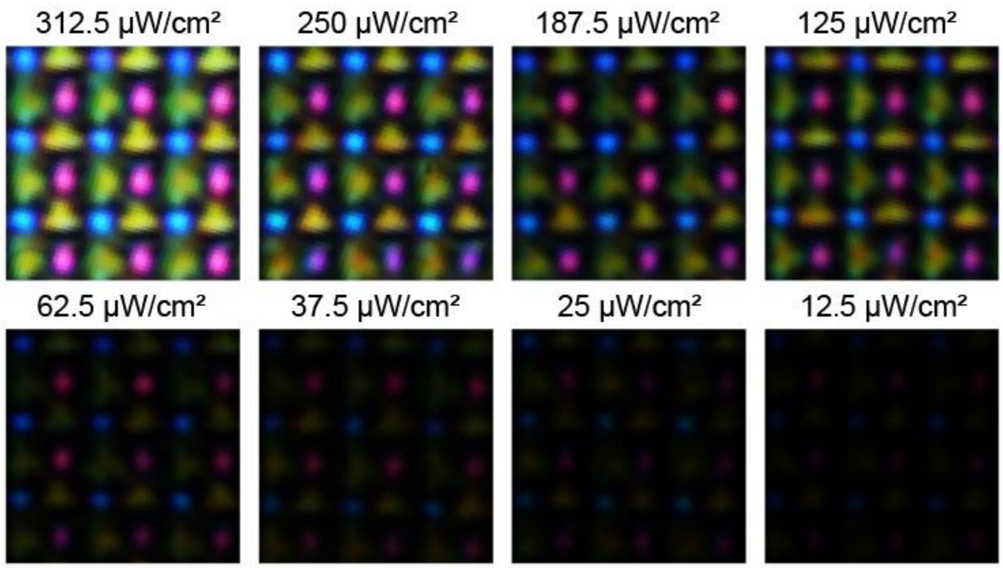

Supplementary Figure 22 Optical microscope images of the fabricated color router (CR) recorded under broadband white-light illumination at different incident power densities, as labeled above each panel. The images were acquired in transmission mode using a Nikon Eclipse LV100ND microscope equipped with a 100× objective lens (NA = 0.9). For the imaging test, the aperture of the halogen lamp was reduced to improve the directionality of the broadband illumination. An attenuator was inserted in the illumination path to vary the incident light level, and the corresponding power density was measured using an Ophir Nova power meter at the sample plane over a detection area of 80 cm^2.

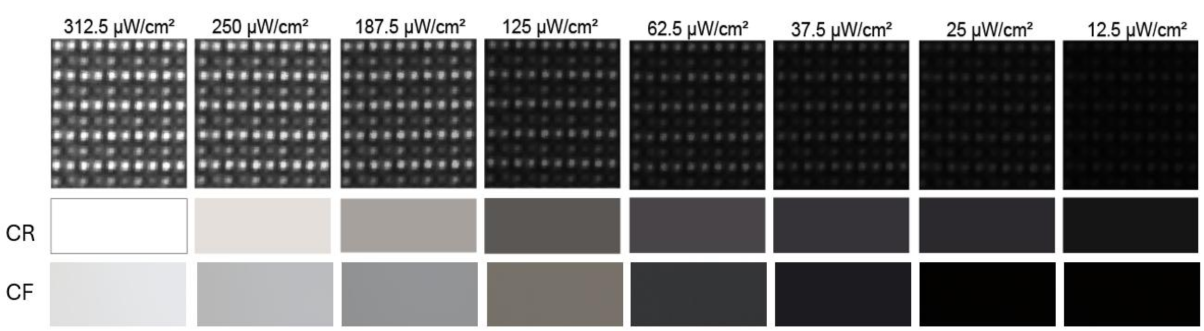

Supplementary Figure 23. **Low-light imaging comparison between the LRI-CR and conventional CF.**

Experimental images captured using the LRI-CR and conventional color filter (CF) under different illumination intensities, ranging from 312.5 to 12.5 μW/cm². The top row shows the projected test pattern under each illumination condition, while the middle and bottom rows show the corresponding reconstructed images obtained with the LRI-CR and CF, respectively. As the illumination intensity decreases, the LRI-CR maintains higher image brightness and more discernible spatial features than the CF, demonstrating its improved photon-utilization capability and potential advantage for low-light imaging.

Supplementary Note 20: Post-process to improve the accuracy

For each RGGB unit cell, the monochrome sensor records grayscale intensities corresponding to the routed spectral components in the R, G_1, G_2, B sub-pixel regions. The recorded intensity in channel k can be expressed as

$$I_k = \int_\lambda S(\lambda)O(\lambda)R_k(\lambda)Q(\lambda)d\lambda$$

Where $S(\lambda)$ is the illumination spectrum, $O(\lambda)$ is the object spectral response, $R_i(\lambda)$ is the spectral routing response of the CR for channel k, $Q(\lambda)$ is the detector quantum efficiency. Th four grayscale values within one RGGB unit cell are then assembled into a measurement vector,

$$\boldsymbol{i} = [I_R, I_G, I_B]^T,$$

We use the projected white color as the normalized white, Normalize:

$$\boldsymbol{c}_{norm} = \frac{\boldsymbol{i}}{\boldsymbol{i}_{white}}$$

$$c_{sRGB} = \begin{cases} 12.92\boldsymbol{c}_{norm}, & \boldsymbol{c}_{norm} \leq 0.0031308 \\ 1.055c_{norm}^{1/2.4}, & \boldsymbol{c}_{norm} \geq 0.0031308 \end{cases}$$

The color can be further calibrated by converting into a three-channel RGB vector through a calibrated linear conversion matrix,

$$\boldsymbol{c} = [C_R, C_G, C_B\ ]^T = \boldsymbol{A}c_{sRGB},$$

Given N sets of known color samples, measure the grayscale vector $\boldsymbol{i}^{(j)}$output by the router, the corresponding RGB value is $\boldsymbol{c}^{(j)}$, the least squares method can then be used to solve the problem. And the calibrated color is used in the sRGB range. This procedure can be used to correct the color and make it closer to the real field.

$$\boldsymbol{A} = \underset{A}{\operatorname{argmin}} \sum_{j=1}^{N} \left\| \boldsymbol{c}^{(j)} - \boldsymbol{A}\boldsymbol{i}^{(j)} \right\|_2^2$$

Overall, the stitching strategy, the developed color matching post process together with careful optical alignment and the limited sensitivity of the device to small non-uniformities, ensures that stitching distortion, accumulated color drift, and illumination non-uniformity do not affect the conclusions of the reconstructed imaging results.

Reference

1. Wang H, Ruan Q, Wang H, Rezaei SD, Lim KT, Liu H*, et al.* Full color and grayscale painting with 3D printed low-index nanopillars. *Nano Letters* 2021, **21**(11)**:** 4721-4729.

2. Cao C, Xia X, Shen X, Wang X, Yang Z, Liu Q*, et al.* Ultra-high precision nano additive manufacturing of metal oxide semiconductors via multi-photon lithography. *Nature Communications* 2024, **15**(1)**:** 9216.

3. Zhang L, Wang C, Zhang C, Xue Y, Ye Z, Xu L*, et al.* High-throughput two-photon 3D printing enabled by holographic multi-foci high-speed scanning. *Nano Letters* 2024, **24**(8)**:** 2671-2679.

4. Rowlands DA. Color conversion matrices in digital cameras: a tutorial. *Optical Engineering* 2020, **59**(11)**:** 110801-110801.